PNAS
www.pnas.org

Supplementary Information for

Rapidly deployable and morphable 3D mesostructures with applications in multi-modal biomedical devices

Fan Zhang[a,b,1], Shupeng Li[c,d,e,1], Zhangming Shen[a,b], Xu Cheng[a,b], Zhaoguo Xue[a,b], Hang Zhang[a,b], Honglie Song[a,b], Ke Bai[a,b], Dongjia Yan[a,b], Heling Wang[c,d,e,2], Yihui Zhang[a,b,2], Yonggang Huang[c,d,e,2]

[a]Key Laboratory of Applied Mechanics of Ministry of Education, Department of Engineering Mechanics, Tsinghua University, Beijing 100084, P.R. China; [b]Center for Flexible Electronics Technology, Tsinghua University, Beijing 100084, P.R. China; [c]Department of Mechanical Engineering, Northwestern University, Evanston, IL 60208, USA; [d]Department of Civil and Environmental Engineering, Northwestern University, Evanston, IL 60208, USA; [e]Department of Materials Science and Engineering, Northwestern University, Evanston, IL 60208, USA

[1]F.Z. and S.L. contributed equally to this work.

[2]To whom correspondence should be addressed. E-mail: helingwang1@gmail.com, or yihuizhang@tsinghua.edu.cn or y-huang@northwestern.edu

This PDF file includes:

Other supplementary materials for this manuscript include the following:

Supplementary Information Text

Finite element analysis. The commercial software ABAQUS was used to design the 3D mesostructures actuated by Lorentz forces, optimize their mechanical performance and analyze their thermal properties.

Modeling the deformation driven by Lorentz force involved the electrics-mechanics coupling of electrical current and structural deformation, which was not directly available in ABAQUS. Therefore, a home-made python script was developed and combined with ABAQUS to model this coupling process. The modeling started with the simulation of the electrical current in the current structural configuration generated by the voltage. The simulation was divided into several loading steps. At the first step, a small portion of the total voltage was applied as the electrical boundary condition in the thermal-electrical module of ABAQUS, with eight-node linearly coupled thermal-electrical elements (DC3D8E). Based on the simulated distribution of current density $\boldsymbol{J}$, the Lorentz force per unit volume was calculated by the python script as $\boldsymbol{F} = \boldsymbol{J} \times \boldsymbol{B}$, where $\boldsymbol{B}$ is the uniform magnetic field. The Lorentz force was then imported into the mechanics module of ABAQUS as the body force, and the actuated structural deformation was simulated with finite-deformation, four-node shell elements (S4R). As the structural configuration changed due to Lorentz force, the current distribution was simulated again to account for this update in configuration. The above process was performed iteratively until convergency, i.e. the configuration of two iterations became the same (within a small tolerance). After convergency, the voltage was increased by a small portion and the above process was repeated until all voltages were applied. Refined mesh was used in all simulation cases to ensure accuracy. All the deformations in the analysis were within elastic limits, therefore, the materials were modeled by linear elastic constitutions. The elastic modulus (E), Poisson's ratio (v) were E_{PI} = 2.5 GPa, v_{PI} = 0.34 for PI, E_{Cu} = 119 GPa, v_{Cu} = 0.34 for copper, E_{Ni} = 200 GPa, v_{Ni} = 0.31 for nickel.

For thermal simulations, eight-node linear heat transfer elements (DC3D8) were applied to both the device and the artificial skin. The device was built in the same geometry as that in the

experiment setup and a body heat flux was applied to the heater. The air convection was applied to each surface to simulate the heat exchange with the surrounding environment. Refined mesh was used in the model, especially the region around the heater and the sensor, to ensure accuracy. The mass density (ρ), thermal conductivity (k) and heat capacity (c) were ρ_{PI} = 1200 kg·m^{-3}, k_{PI} = 1.0 W·m^{-1}·K^{-1}, c_{PI} = 1090 J·kg^{-1}·K^{-1} for PI; ρ_{Cu} = 8960 kg·m^{-3}, k_{Cu} = 397 W·m^{-1}·K^{-1}, c_{Cu} = 386 J·kg^{-1}·K^{-1} for copper. The thermal convection coefficient with air was 25 W·m^{-2}·K^{-1}. The thermal conductivity of PI and the thermal convection coefficient were fitted with experiments on the artificial materials Sylgard 184 and Sylgard 160 and their bilayers.

Derivation of the scaling law for the normalized out-of-plane displacement actuated by Lorentz force. For Eq. 1 in the main text, dimensional analysis suggests that the out-of-plane displacement (deflection) of the suspended serpentine structure (u, see Fig. S4*A*) is inversely proportional to the out-of-plane bending stiffness (Ebh^3 / 12), and is also linearly proportional to the applied Lorentz force (BIL). FEA further shows that for sufficiently large deformation (u / L > 5%), the deflection is inversely proportional to the unit cell length (λ) and the square of the width (b), and linearly proportional to the cube of the serpentine height (H) and the total length (L), which gives

$$\frac{u}{L}=4.6\times10^{-4}\frac{BIL^2H^3}{Eb^2h^3\lambda},\left(\frac{u}{L}>5\%\right), \tag{S1}$$

with the slope 4.6×10^{-4} fitted from FEA. Fig. S4*B* shows FEA validation of Eq. S1. With the baseline values E = 2.5 GPa, h = 7 μm, b = 300 μm, λ= 1800 μm, H = 9120 μm, L = 16200 μm, I = 10 mA, and B = 0.1 T, variation of any of the paramters in Eq. S1 yields approximately the same straight line for the relationship of the normalized out-of-plane displacement (u / L) vs. the material combination $\frac{BIL^2H^3}{Eb^2h^3\lambda}$.

Derivation of the scaling law for the critical current of state switching. For Eq. 2 in the main text, dimensional analysis suggests that the critical force $(BIL)_c$ for the state switching of the buckled serpentine ribbon is proportional to the out-of-plane bending stiffness (Ebh^3 / 12). FEA suggested that the critical force is inversely proportional to $L^{0.5}$ and $H^{2.5}$, and linearly proportional to λ, which gives

$$\left(BIL\right)_c = \alpha \frac{Ebh^3 \lambda}{L^{0.5} H^{2.5}}, \tag{S2}$$

or equivalently

$$I_c = \alpha \frac{Ebh^3 \lambda}{BL^{1.5} H^{2.5}}, \tag{S3}$$

where the slope α depends on the prestrain used to buckle the serpentine ribbon in the mechanics-guided 3D assembly and is fitted from FEA. For a biaxial prestrain ($\varepsilon_{x\text{-pre}}$ = 50% and $\varepsilon_{y\text{-pre}}$ = 11%), α = 5.7. Fig. S8*B* shows FEA validation of Eq. S3. With the baseline values E = 2.5 GPa, h = 7 μm, b = 300 μm, λ = 1800 μm, H = 9120 μm, L = 16200 μm and B = 0.1 T, variation of any of the paramters in Eq. S3 yields approximately the same straight line for the relationship of the critical current (I_c) vs. the material combination $\frac{Ebh^3 \lambda}{BL^{1.5} H^{2.5}}$.

The sensing depth analysis. For the analytical model consisting of a heater on a semi-infinite, homogeneous medium (Fig. S13*B*), the temperature below the heater (r = 0, with r being the distance to the center of the heater) is (1)

$$\Delta T = \frac{2q\sqrt{\alpha t}}{k}\left(\text{ierfc}\left(\frac{z}{2\sqrt{\alpha t}}\right) - \text{ierfc}\left(\frac{\sqrt{z^2 + a^2}}{2\sqrt{\alpha t}}\right)\right), \tag{S4}$$

where q is the heat flux, t is the heating time, α and k are the medium thermal diffusivity and conductivity respectively, z is the position under the center of the heater and a is the radius of the heater. The function ierfc( ) is the inverse complementary error function.

The normalized temperature with respect to the maximum temperature at $z = 0$ [$\Delta T_{max} = \Delta T(z = 0)$] is

$$\Delta T_{\text{normalized}} = \frac{\Delta T}{\Delta T_{\max}} = \frac{\text{ierfc}\left(\frac{a}{2\sqrt{\alpha t}}\frac{z}{a}\right) - \text{ierfc}\left(\frac{a}{2\sqrt{\alpha t}}\sqrt{\left(\frac{z}{a}\right)^2 + 1}\right)}{\frac{1}{\sqrt{\pi}} - \text{ierfc}\left(\frac{a}{2\sqrt{\alpha t}}\right)} = F\left(\frac{a^2}{\alpha t}, \frac{z}{a}\right), \quad \text{(S5)}$$

as shown in Fig. S13*C*. With a sufficiently long time (t) such that $a^2/(\alpha t)$ tends to zero, $\Delta T_{\text{normalized}}$ can be simplified to

$$\Delta T_{\text{normalized}} = \sqrt{\left(\frac{z}{a}\right)^2 + 1} - \frac{z}{a}, \quad \text{(S6)}$$

which is the single-variable function of z/a. This analysis suggests that for sufficiently long heating time (t), the heat penetration depth is independent of the material property and increases with the heater size (a).

For the parameters used in the device and the artificial skin shown in Fig. 5*A*, $a \approx 0.33$ mm, $\alpha \approx 0.15$ mm^2/s and $t \approx 30$ s, such that $a^2/(\alpha t)$ in Eq. S5 is sufficiently small (≈ 0.02) and has a negligible effect on the heat penetration depth. Therefore, the heater size plays a major role in determining the heat penetration depth of the device.

Error analysis for the thermal conductivities. Using the measurement of the two sensing units of the device shown in Fig. 5*A*, the thermal conductivity k_{top} of the top layer and k_{bottom} of the bottom layer can be solved from two coupled equations, i.e.

$$\Delta T_1 = G_1\left(k_{\text{top}}, k_{\text{bottom}}\right), \quad \text{(S7)}$$

$$\Delta T_2 = G_2\left(k_{\text{top}}, k_{\text{bottom}}\right). \quad \text{(S8)}$$

The nonlinear functions G_1 and G_2 are obtained by FEA with the variables in the range $0.27\,\mathrm{W/(m\cdot K)} \le k_{top}, k_{bottom} \le 0.60\,\mathrm{W/(m\cdot K)}$, which are the typical range of the thermal conductivity of skin (2). Numerical results showed that k_{top} and k_{bottom} can be solved from Eqs. S7 and S8 successfully.

The error in the temperature measurement of the device δT leads to errors in the determined thermal conductivities k_{top} and k_{bottom}. For $\Delta T_1 \pm \delta T$ and $\Delta T_2 \pm \delta T$, the coupled equations (Eqs. S7 and S8) are solved again and the differences in the solutions give the errors. For δT = 0.1 K, the maximum relative errors in the predictions of k_{top} and k_{bottom} are derived as 3% and 10%, respectively (Table S1 and S2).

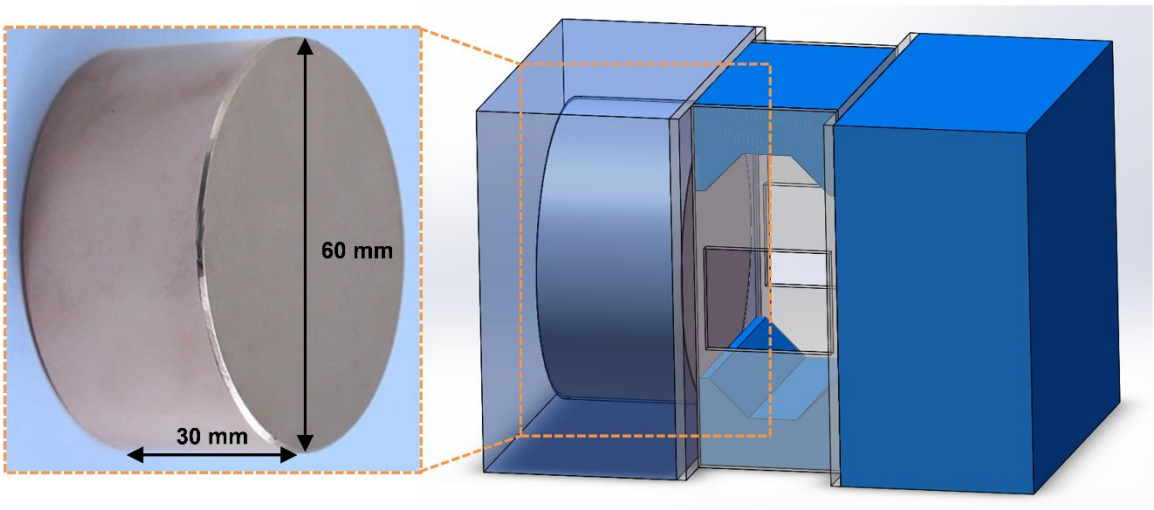

Fig. S1. Schematic illustration of a customized platform with a couple of disk-shaped magnets.

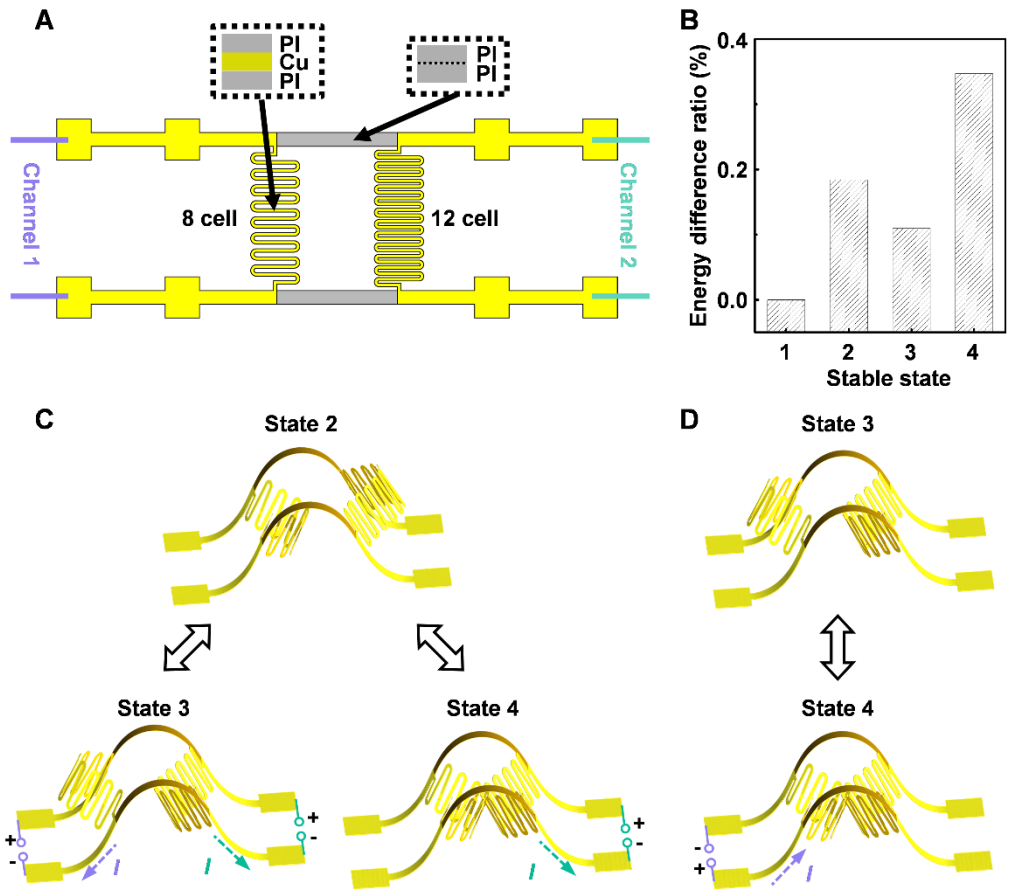

Fig. S2. (A) Illustration of two independently addressable channels of the deployable 3D ribbon mesostructure. (B) The energy difference ratios for four stable states of the deployable 3D ribbon mesostructure. (C) Schematic illustration that shows the transformation between State 2 and State 3 or 4 by applying Lorentz forces. (D) Schematic illustration that shows the transformation between State 3 and State 4 by applying Lorentz forces.

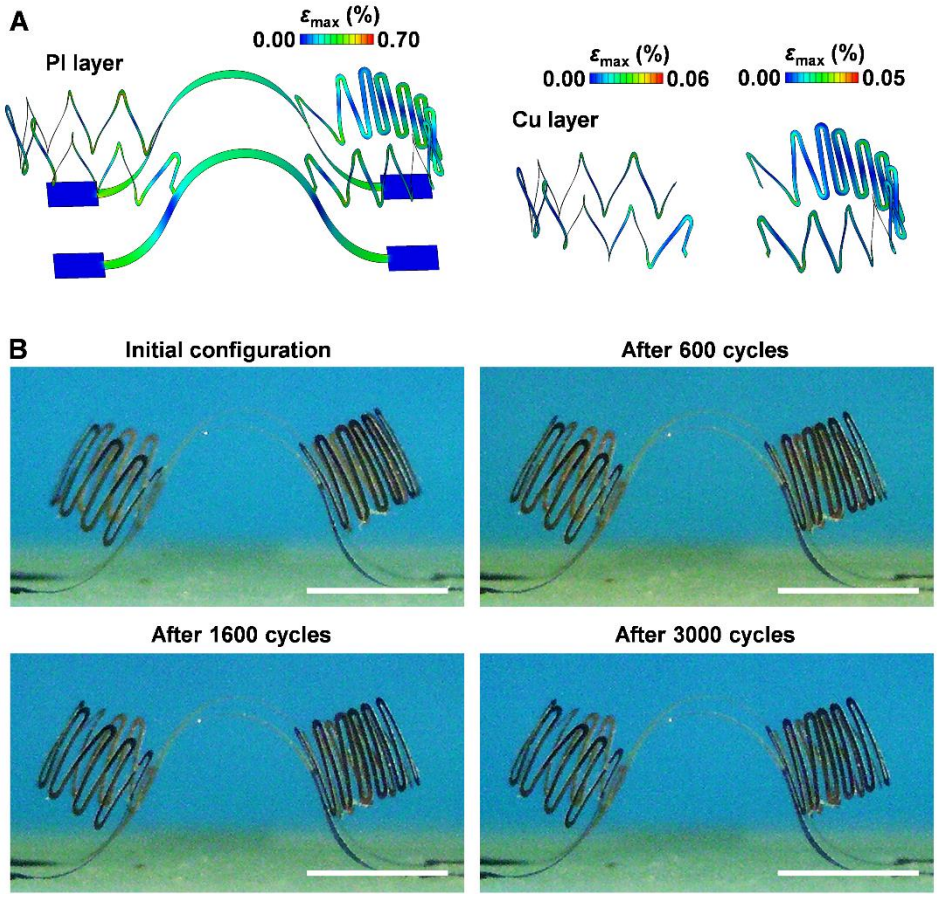

Fig. S3. (A) FEA results for a deployable 3D ribbon mesostructure show the distribution of the maximum principal strain. (B) Cyclic testing of a deployable 3D ribbon mesostructure actuated by Lorentz forces at a frequency of ~ 2 Hz for 3000 cycles. The four images correspond to the initial state, and the states after 600, 1600, and 3000 cycles. Scale bars, 2 mm.

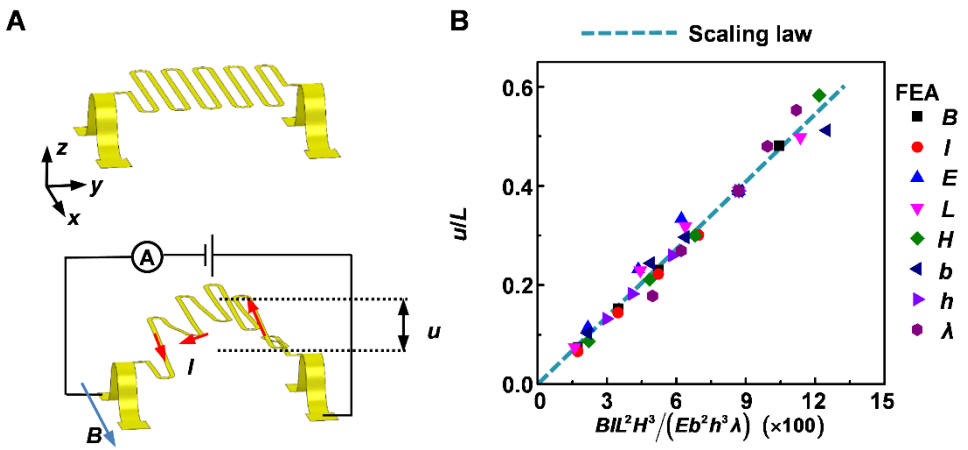

Fig. S4. (A) FEA result that shows the deformation process of a suspended serpentine mesostructure by applying external magnetic field and current. (B) Dependence of the normalized out-of-plane displacement on the geometry, material, electricity, and magnetic field parameters.

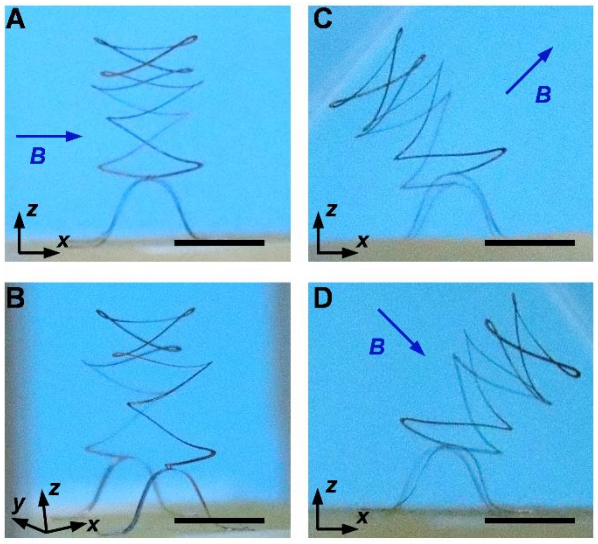

Fig. S5. Deformed configurations of a suspended serpentine mesostructure with different directions of the magnetic field. Scale bars, 5 mm.

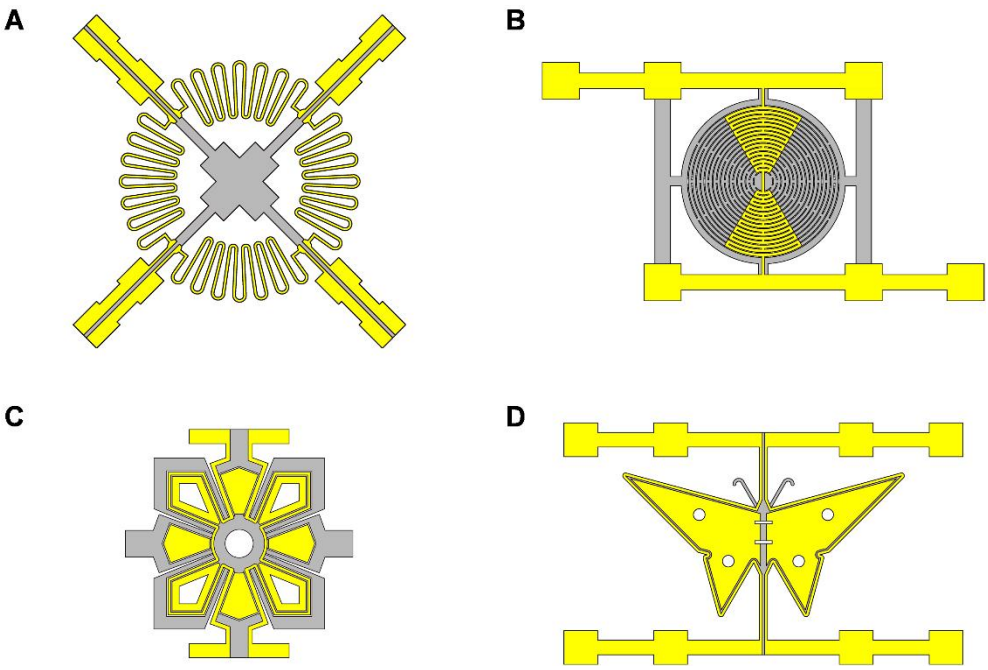

Fig. S6. 2D precursors of the 3D mesostructures in Fig. 2 *B-D* and *F*.

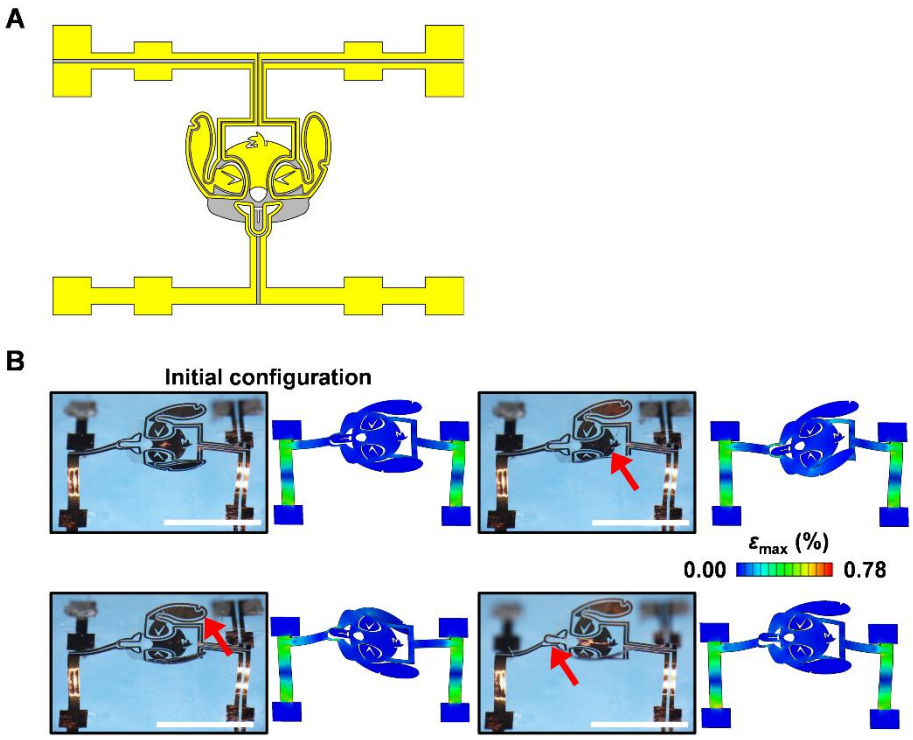

Fig. S7. (A) 2D precursor of a cartoon dog face. (B) Optical images and FEA results of the initial configuration and three temporary configurations actuated by Lorentz forces. Scale bars, 4 mm.

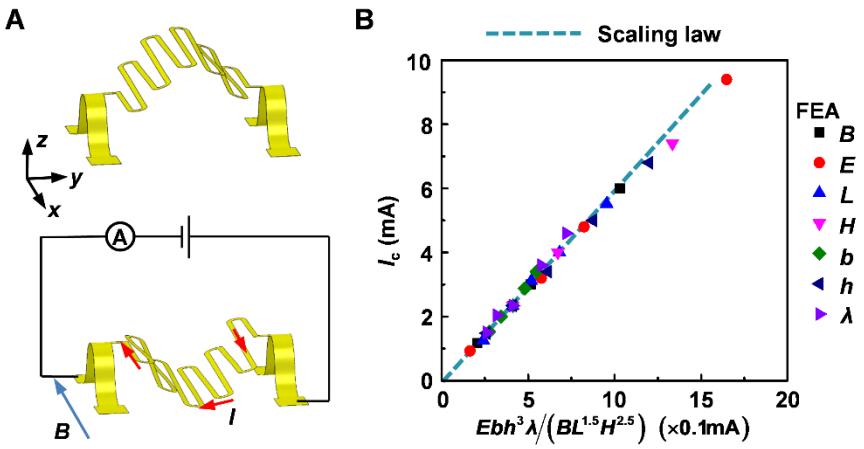

Fig. S8. (A) FEA result that shows the mode transition of a suspended serpentine mesostructure by applying external magnetic field and current. (B) Dependence of the critical current on the geometry, material, and magnetic field parameters.

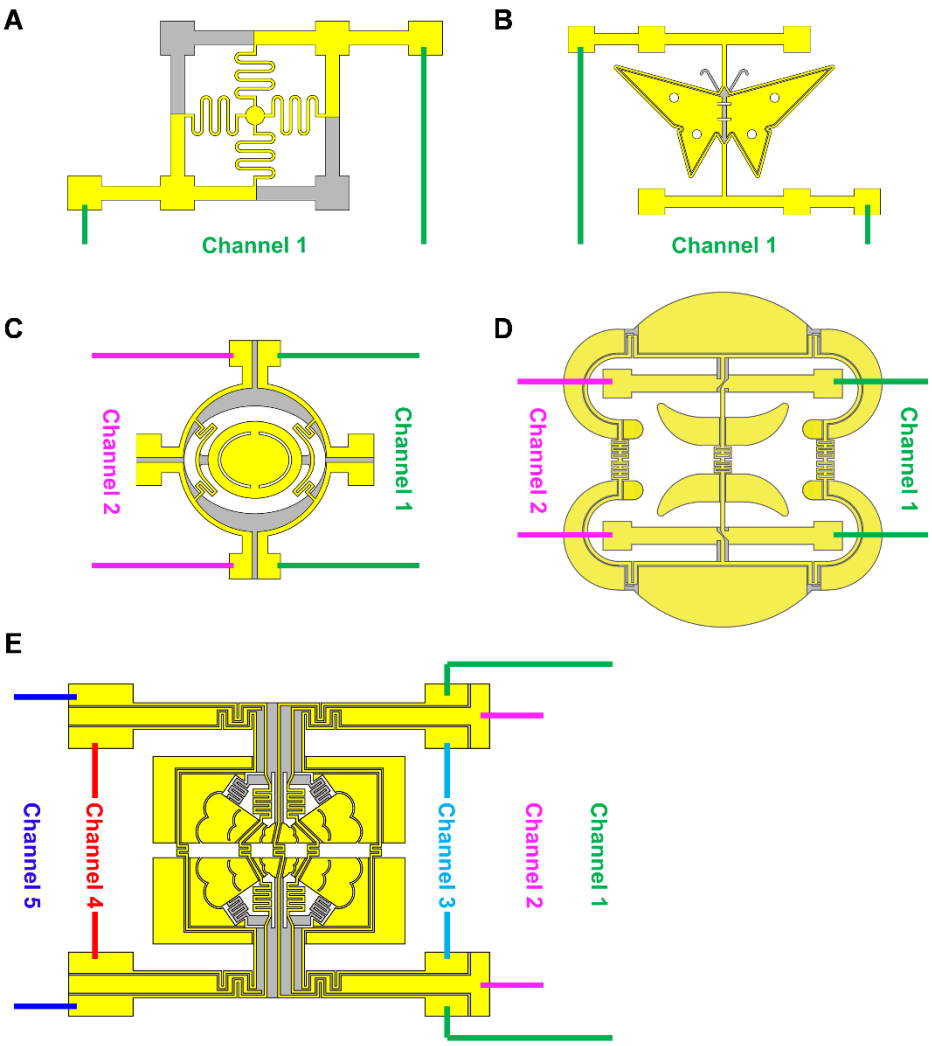

Fig. S9. 2D precursors of the reconfigurable 3D mesostructures in Fig. 3 *C-G*.

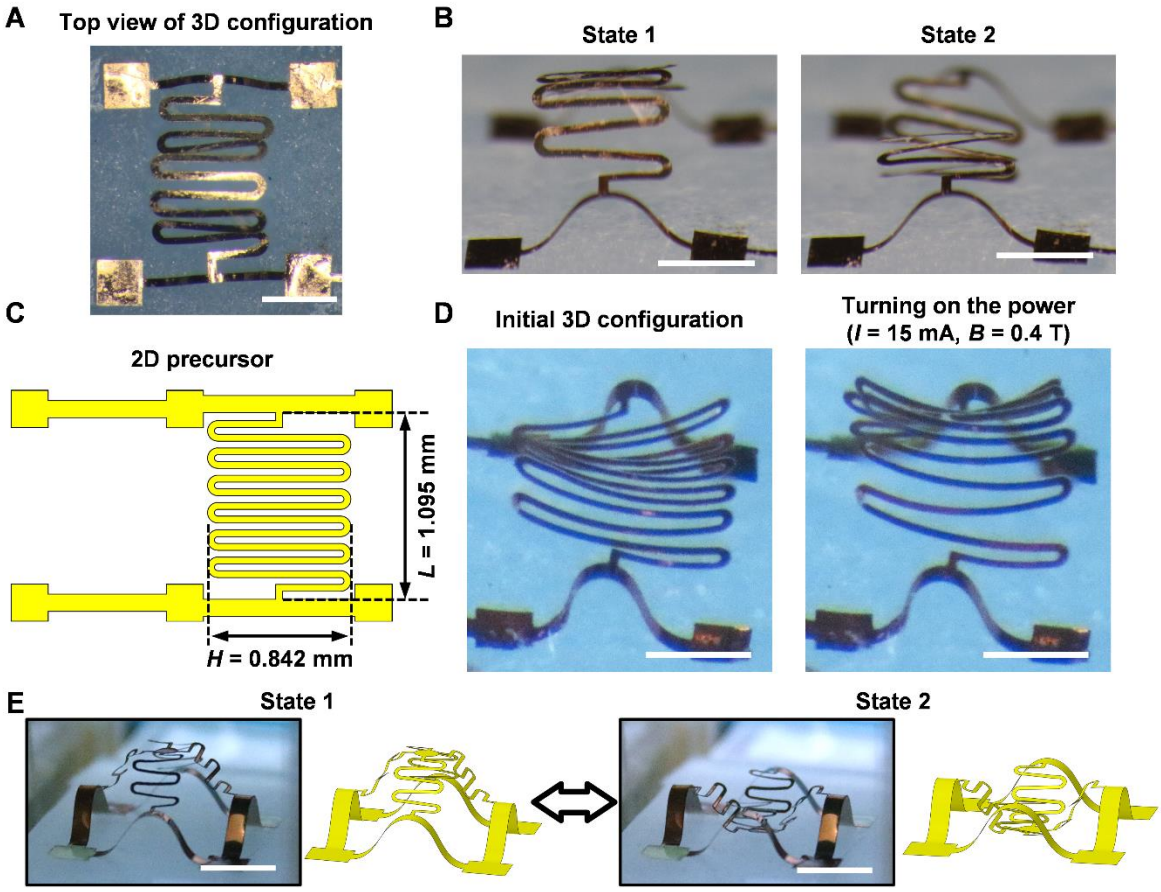

Fig. S10. (A-B) Optical images of a suspended serpentine mesostructure (corresponding to Fig. 3*A*) at a smaller scale. Scale bars, 1 mm. (C) 2D precursor of the suspended serpentine mesostructure with L = 1.095 mm. (D) Optical images of the suspended serpentine mesostructure that show the initial 3D configuration and deformed configuration by applying magnetic field (B = 0.4 T) and current (I = 15 mA). Scale bars, 400 μm. (E) Optical images and FEA results of a bistable mesostructure (corresponding to Fig. 3*C*) at a larger scale. Scale bars, 5 mm.

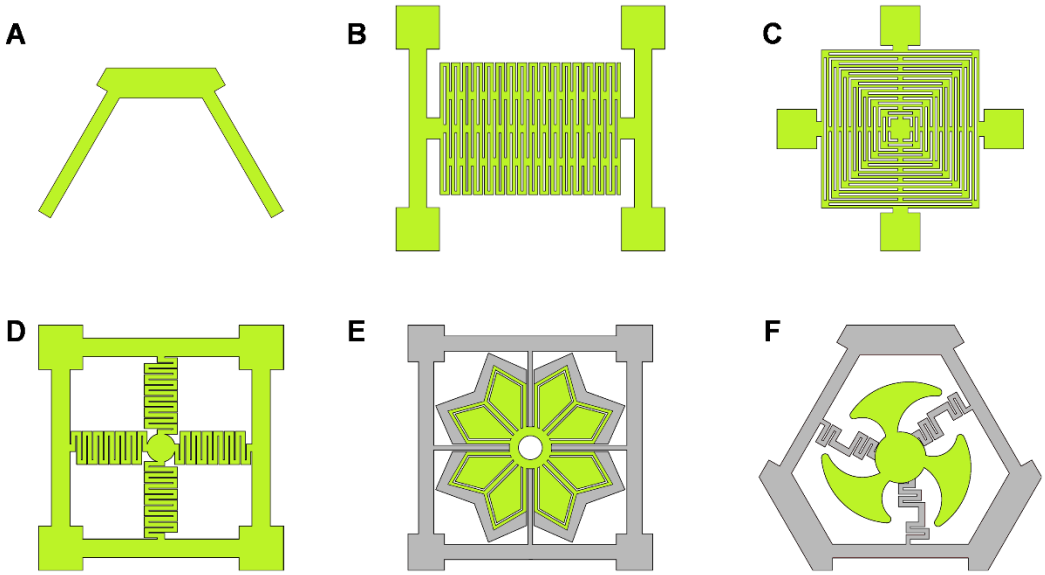

Fig. S11. 2D precursors of the deployable and reconfigurable 3D mesostructures with magnetic materials in green regions corresponding to Fig. 4 *A*-*G*.

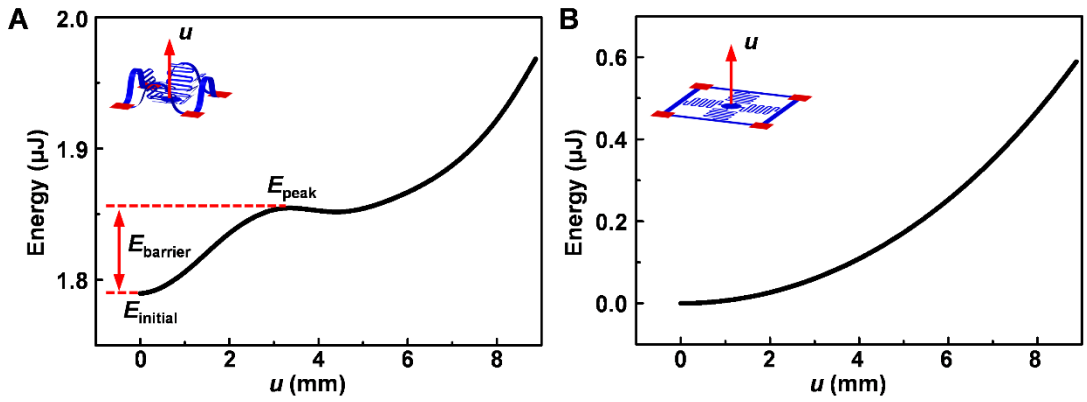

Fig. S12. Strain energy as a function of the out-of-plane displacement (*u*) for the device with suspended state (*A*) and flat state (*B*). The insets show the initial configuration.

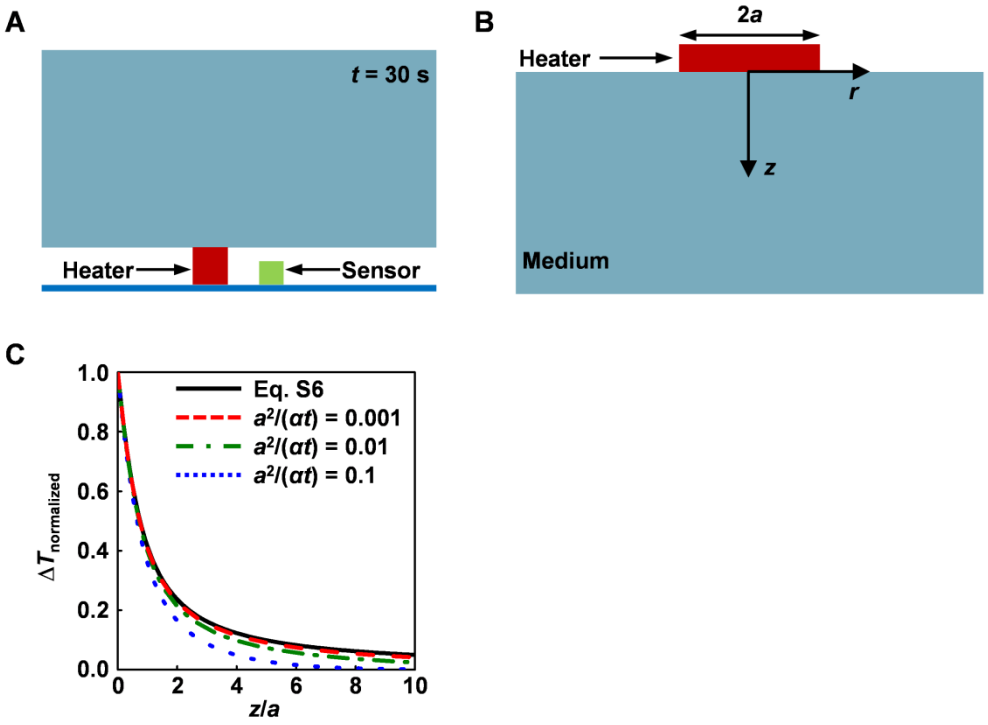

Fig. S13. (A) Cross-sectional illustration of the simulation model for analyzing the heat penetration depth. (B) Schematic illustration of a heater on a semi-infinite, homogeneous medium. (C) The normalized temperature ($\Delta T_{normalized}$) as a function of z/a with different $a^2/(\alpha t)$.

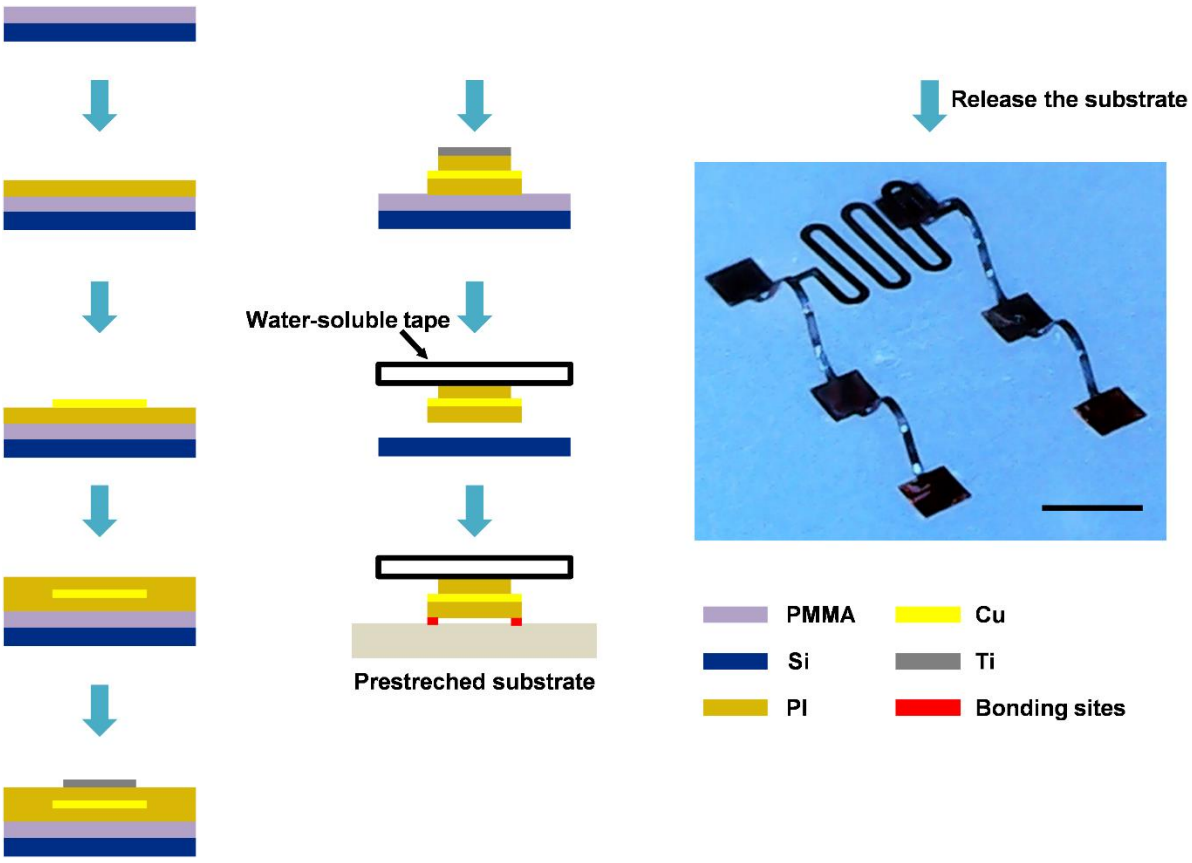

Fig. S14. Schematic illustration of the fabrication process of 3D mesostructures by photolithography**.** Scale bars, 1 mm.

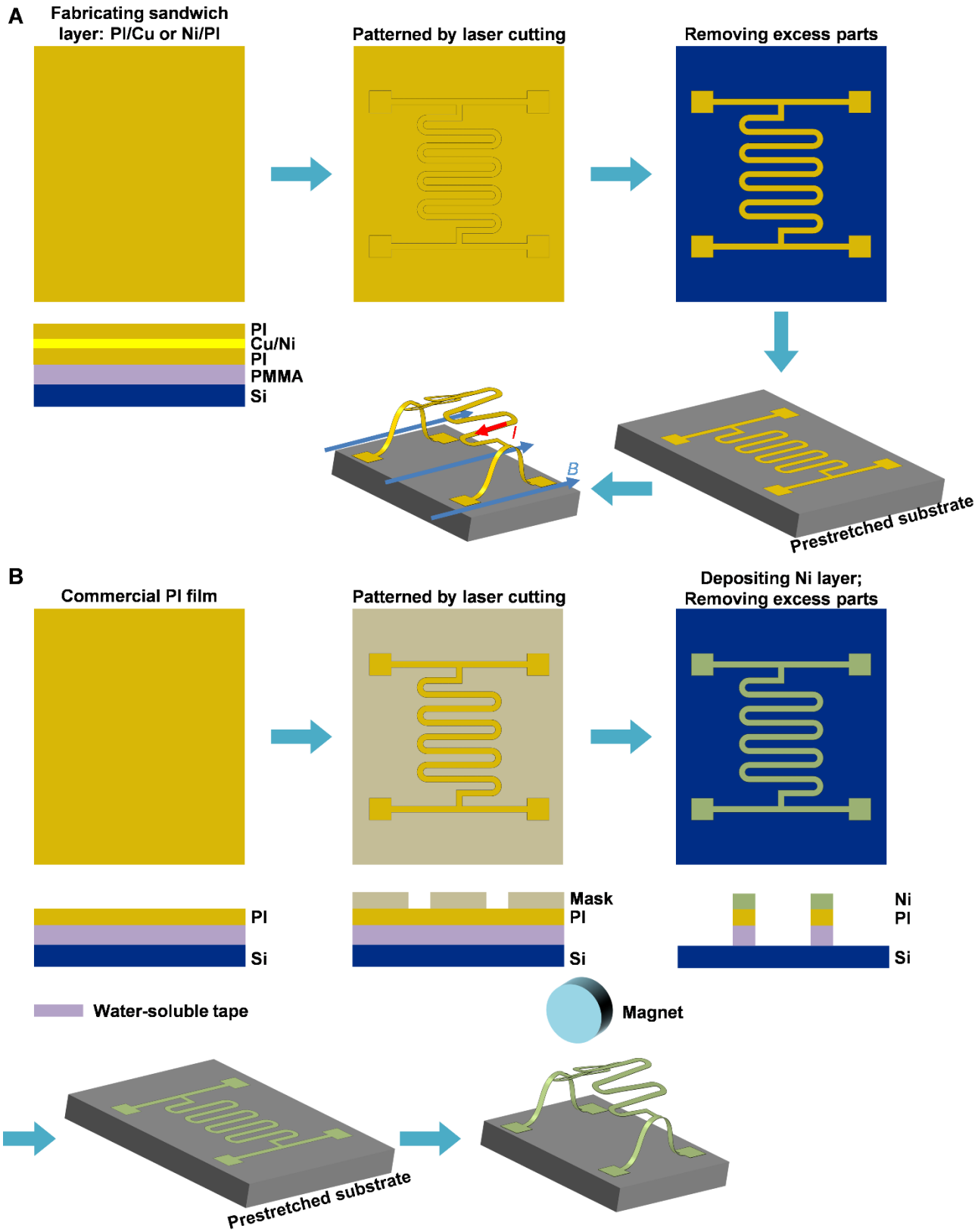

Fig. S15. Schematic illustration of the fabrication process of 3D mesostructures by laser cutting.

Table S1. Relative errors for the thermal conductivity of top layer in a bilayer material.

k_2 \ k_1	0.3	0.4	0.5	0.6
0.3	0.013	0.013	0.010	0.005
0.4	0.013	0.008	0.008	0.010
0.5	0.013	0.015	0.014	0.007
0.6	0.027	0.028	0.032	0.028

Table S2. Relative errors for the thermal conductivity of bottom layer in a bilayer material.

k_2 \ k_1	0.3	0.4	0.5	0.6
0.3	0.063	0.073	0.083	0.097
0.4	0.078	0.095	0.095	0.090
0.5	0.076	0.076	0.088	0.100
0.6	0.103	0.062	0.073	0.083

Movie S1 (separate file). Reconfigurable and deployable 3D mesostructure actuated by Lorentz forces.

SI References

1. Carslaw HS & Jaeger JC, *Conduction of heat in solids* (Oxford University Press, Oxford, UK, 1986) Second Ed, p 520.
2. Krishnan S, et al., Multimodal epidermal devices for hydration monitoring. *Microsystems & Nanoengineering* **3**, 17014 (2017).